physica status solidi rrl
www.pss-rapid.com

Epitaxial AlBN/β-Nb_2N Ferroelectric/Superconductor Heterostructures

Chandrashekhar Savant, Thai-Son Nguyen, Saurabh Vishwakarma, Joongwon Lee, Anand Ithepalli, Yu-Hsin Chen, Kazuki Nomoto, Farhan Rana, David J. Smith, Huili Grace Xing, and Debdeep Jena*

We report the growth of AlBN/β-Nb_2N nitride epitaxial heterostructures in which the AlBN is ferroelectric, and β-Nb_2N with metallic resistivity ≈40 μΩ cm at 300 K becomes superconducting below $T_C \approx 0.5$ K. Using nitrogen plasma molecular beam epitaxy, we grow hexagonal β-Nb_2N films on c-plane Al_2O_3 substrates, followed by wurtzite AlBN. The AlBN is in epitaxial registry and rotationally aligned with the β-Nb_2N, and the hexagonal lattices of both nitride layers make angles of 30° with the hexagonal lattice of the Al_2O_3 substrate. The B composition of the AlBN layer is varied from 0 to 14.7%. It is found to depend weakly on the B flux, but increases strongly with decreasing growth temperature, indicating a reaction rate-controlled growth. The increase in B content causes a non-monotonic change in the a-lattice constant and a monotonic decrease in the c-lattice constant of AlBN. Sharp, abrupt epitaxial AlBN/β-Nb_2N/Al_2O_3 heterojunction interfaces and close symmetry matching are observed by transmission electron microscopy. The observation of ferroelectricity and superconductivity in epitaxial nitride heterostructures opens avenues for novel electronic and quantum devices.

1. Introduction

Nitrogen-containing crystalline layers with semiconducting, metallic, superconducting, piezoelectric, ferroelectric, high-K dielectric, and optical properties[1] are pivotal in advancing photonic, acoustic, quantum, and electronic devices.[1–4] The ultrawide direct energy bandgap and piezoelectric properties of AlN have made it the material of choice for deep-ultraviolet photonic devices and RF BAW filters.[1,5–7] AlN is pyroelectric and not ferroelectric.[8,9] The current understanding is that spontaneous polarization is locked in one direction and cannot be switched by an external electric field below the breakdown voltage.[8–11] Recently, high-K dielectric properties and ferroelectricity were discovered in AlN substituted with isovalent B, Sc, and Y, enabling new functionalities and applications.[9,10,12–15] Compared to other alternatives, the B alloying route to AlN differs in two essential ways: a) the ultrawide bandgap of AlN is retained;[9,16–20] and b) the smaller lattice parameter and stronger B-N bond are expected to offer higher thermal conductivity, and more resistance to thermal and chemical oxidation.[1,21–24] Thus, AlBN is of interest for deep UV optoelectronics[6,16] and high-power electronics,[17] especially in extreme temperature, voltage, and radiation environments.[1,21–27]

A nonvolatile memory effect of superconductivity in oxide ferroelectric/superconductor heterostructures has been observed by the modulation of superconductor charge density and T_C with ferroelectric polarization.[28–32] To date, ferroelectric/superconductor nitride heterostructures have not been realized. Hexagonal β-Nb_2N with metallic and superconducting properties is a new platform for the epitaxial growth of ferroelectric AlBN films due to its symmetry and lattice-matching with AlN. Its high thermal stability up to ≈900–1100 °C is conducive to AlBN film growth.[33–36] Owing to its ultrahigh vacuum nature, elemental purity of sources, and low substrate damage from the low kinetic energy of evaporated molecular beams, plasma-assisted molecular beam epitaxy (PAMBE) exploits unique growth dynamics to yield films of high crystal quality. Prior studies of the MBE growth of AlBN have been reported by: a) ammonia-MBE[37] with up to 6% B; b) a BBr_3 gaseous precursor-based PAMBE[38] which reported up to 5%–6% B, with clustering of

C. Savant, T.-S. Nguyen, A. Ithepalli, Y.-H. Chen, H. G. Xing, D. Jena
Department of Materials Science and Engineering
Cornell University
Ithaca, NY 14853, USA
E-mail: cps259@cornell.edu

S. Vishwakarma
School for Engineering of Matter, Transport and Energy
Arizona State University
Tempe, Arizona 85287, USA

J. Lee, K. Nomoto, F. Rana, H. G. Xing, D. Jena
School of Electrical and Computer Engineering
Cornell University
Ithaca, NY 14853, USA

D. J. Smith
Department of Physics
Arizona State University
Tempe, Arizona 85287, USA

H. G. Xing, D. Jena
Kavli Institute at Cornell for Nanoscale Science
Cornell University
Ithaca, NY 14853, USA

The ORCID identification number(s) for the author(s) of this article can be found under https://doi.org/10.1002/pssr.202400157.

DOI: 10.1002/pssr.202400157

B and possible Br contamination; and c) using an energetic neutral atom beam lithography and epitaxy-MBE[39] which reported up to 3% B.

Here we report the PAMBE growth of AlBN films on β-Nb_2N using a boron effusion cell and a nitrogen plasma source with 0%–15% B concentration in wurtzite phase. The effect of various growth parameters on controlling the B content of AlBN and the crystal structure and epitaxial registry of the AlBN/β-Nb_2N film heterostructures with the substrate are found. Ferroelectricity in the MBE-grown AlBN films and superconductivity of the β-Nb_2N are observed in the AlBN/β-Nb_2N/Al_2O_3 heterostructures.

2. Results and Discussion

2.1. Epitaxial AlBN/β-Nb_2N Heterostructures Grown by MBE

Figure 1a shows the schematic layer structure of AlBN/β-Nb_2N film heterostructures grown by nitrogen plasma-assisted MBE on a c-plane sapphire substrate. Hexagonal β-Nb_2N is the most metal-rich phase of niobium nitride. It is stabilized and made phase-pure by using a high substrate thermocouple (TC) temperature of 1150 °C during MBE growth. Nb_2N layers of ≈50 nm thickness were first grown, followed by deposition of ≈200 nm AlBN films at substrate TC temperatures ranging from 600 to 900 °C and B fluxes of ≈10^{-8} torr, as discussed in the next section. Since N exhibits a thermodynamic preference to bond to Al rather than B,[40] the AlBN films in this study were grown in N-rich conditions with III/V flux ratio of ≈0.8. A control AlN/β-Nb_2N sample was also grown on a sapphire substrate without supplying boron. Figure 1b shows that a $10 \times 10\ \mu m^2$ AFM micrograph of a 200-nm-thick ≈14.7% B containing AlBN/β-Nb_2N/Al_2O_3 sample exhibits ≈5 nm rms roughness. Comparable morphology was seen in all AlBN/β-Nb_2N/Al_2O_3 samples in this study. The control β-Nb_2N/Al_2O_3 sample without the AlBN layer showed an rms roughness of 0.43 nm.

Figure 1c shows the evolution of RHEED patterns collected during the MBE growth of AlBN/β-Nb_2N heterostructures along the sapphire $[1\bar{1}00]$ zone axis, i.e., at a constant in-plane phi rotational angle of the substrate. Nucleation of a twin cubic δ-NbN was observed during the initial minute of the niobium nitride film growth, as indicated by the twin cubic domain RHEED pattern with two separate overlaid <1$\bar{1}$0> zone axes, originating from pairs of {111} and {002} families of planes.[33,41] Following this, the β-Nb_2N film was observed to grow with a streaky RHEED diffraction pattern along the $[11\bar{2}0]$ zone axis, suggesting a smooth hexagonal phase film. At a fixed in-plane phi rotational angle of the substrate, the $[11\bar{2}0]$ zone axis of β-Nb_2N film is parallel to the sapphire $[1\bar{1}00]$ zone axis, indicating the growth of β-Nb_2N films at 30° basal in-plane rotation alignment with the sapphire substrate. During the subsequent AlBN film growth, a spotty RHEED pattern is observed, as shown in top Figure 1c for the 14.7% B containing AlBN film. The observed RHEED diffraction spots for AlBN film along the $[11\bar{2}0]$ zone axis indicate Bragg reflections corresponding to first-order 1×1 reconstruction for the wurtzite phase structure.[42] All AlBN films grown in this study show similar spotty wurtzite RHEED patterns, indicating a three-dimensional growth mode for the nitrogen-rich growth conditions used here for B incorporation in AlBN films.[42,43] The wurtzite phase RHEED pattern persists throughout the AlBN film growth. At a fixed in-plane phi rotational angle of the sample, the $[11\bar{2}0]$ zone axis of the AlBN film is parallel to the β-Nb_2N $[11\bar{2}0]$ zone axis, indicating that the AlBN films are symmetrically matching

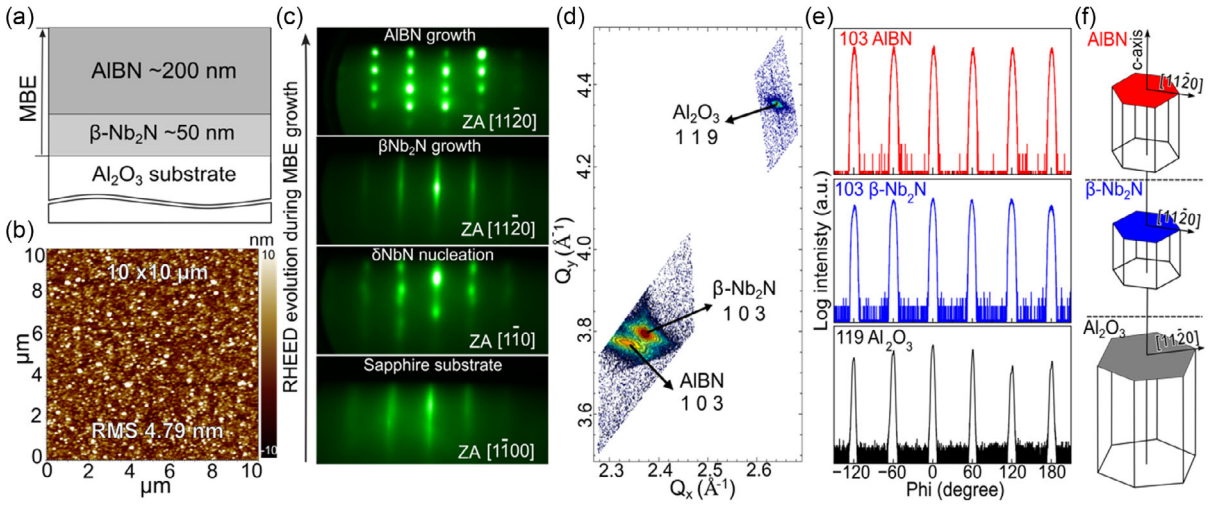

Figure 1. Epitaxial AlBN/β-Nb_2N heterostructures grown by MBE. a) Schematic of sample heterostructure with epitaxial AlBN/ β-Nb_2N films grown by MBE on sapphire substrate, b) $10 \times 10\ \mu m^2$ AFM micrograph of ≈200 nm AlBN film sample containing 14.7% B, c) RHEED evolution during heterostructure growth along the substrate $[1\bar{1}00]$ zone axes, showing the epitaxial nucleation and growth of Nb_xN and AlBN films, d) XRD-RSM map showing 103 AlBN, 103 β-Nb_2N and 119 Al_2O_3 Bragg reflections for sample containing 14.7% B, e) Symmetric phi scans of 103 AlBN, 103 β-Nb_2N and 119 Al_2O_3 Bragg reflections indicating six-fold symmetry and epitaxial registry of AlBN, β-Nb_2N films with the sapphire substrate, and f) Schematic illustration of rotational alignments of the unit cells of AlBN, β-Nb_2N, and Al_2O_3 indicating a good lattice symmetry matching between AlBN and Nb_2N films. A 30° alignment observed in the RHEED zone axes and in the in-plane projections of the asymmetric XRD-RSM, Phi scans indicate a 30° rotational alignment between the hexagonal basal in-planes of AlBN and β-Nb_2N, with that of Al_2O_3.

with the β-Nb_2N films with zero degrees in-plane rotational orientation. However, at a fixed in-plane phi rotational angle of the sample, the $[11\bar{2}0]$ zone axis of the AlBN and the $[11\bar{2}0]$ zone axis of the β-Nb_2N are parallel to the sapphire $[1\bar{1}00]$ zone axes. Since the crystallographic $[11\bar{2}0]$ and $[1\bar{1}00]$ axes in a hexagonal basal plane are separated by a 30° rotation, this indicates that the AlBN and the β-Nb_2N films grew at a 30° basal in-plane rotational alignment with the sapphire substrate.

Figure 1d shows the measured X-Ray diffraction reciprocal space map (XRD-RSM) peaks showing 103 AlBN, 103 β-Nb_2N, and 119 Al_2O_3 Bragg reflections. The 103 Bragg reflection of 14.7% B containing AlBN is close to the β-Nb_2N 103 Bragg reflection and far from the Al_2O_3 119 Bragg reflections implying AlBN is of wurtzite phase and the hexagonal phases of β-Nb_2N films and Al_2O_3 substrate. The XRD-RSM maps shown in Figure 1d were collected at a fixed phi rotation of the sample with the X-Ray beam along Al_2O_3 $[11\bar{2}0]$ crystallographic directions. Only the allowed peaks corresponding to the $[10\bar{1}0]$ Bragg reflections of the AlBN and β-Nb_2N films and the $[11\bar{2}0]$ Bragg reflections of the Al_2O_3 were observed at this fixed phi rotation. Other Bragg peaks, such as $[11\bar{2}0]$ were not observed at this fixed phi position, indicating that the AlBN and β-Nb_2N films grew in an epitaxial relationship with the substrate. XRD-RSM maps of other AlBN/β-Nb_2N/Al_2O_3 samples used in this study (not shown) have a similar diffraction pattern, indicating similar crystal structure and epitaxial registry.

To confirm the epitaxial registry and the in-plane rotational alignment between films and substrate, skew-geometry phi-scans of asymmetric AlBN 103, β-Nb_2N 103, and Al_2O_3 119 reflections were performed as shown in Figure 1e for samples containing 14.7% B. Six peaks at the same positions indicate the 6-fold symmetry and the epitaxial registry of the AlBN, and β-Nb_2N films with Al_2O_3 substrate. The asymmetric AlBN 103 and β-Nb_2N 103 and Al_2O_3 119 peaks originate from diffraction from $\{10\bar{1}3\}$ AlBN, $\{10\bar{1}3\}$ β-Nb_2N and $\{11\bar{2}9\}$ Al_2O_3 sets of crystallographic planes with in-plane projection normals along $<10\bar{1}0>$ AlBN, $<10\bar{1}0>$ β-Nb_2N and $<11\bar{2}0>$ Al_2O_3 crystallographic directions. AlBN 103 and β-Nb_2N 103 and Al_2O_3 119 peaks coincide at similar in-plane phi rotational angle of the sample, i.e., at 0°, suggesting that the $<10\bar{1}0>$ crystallographic axes of the AlBN film, and the β-Nb_2N films are parallel to the $<11\bar{2}0>$ Al_2O_3 crystallographic axes. Since the crystallographic $<10\bar{1}0>$ and $<11\bar{2}0>$ axes in a hexagonal basal plane are separated by a 30° rotation, this confirms that the AlBN and the β-Nb_2N have a 0-degree basal in-plane rotational alignment with each other, while they have a 30° basal in-plane rotational alignment with the sapphire substrate. Similar 6-fold symmetry and epitaxial registry were also observed for other samples. A schematic illustration of the unit cells of AlBN, β-Nb_2N, and Al_2O_3 is shown in Figure 1f indicating good lattice symmetry matching between AlBN and β-Nb_2N films. The growth directions of AlBN and β-Nb_2N are along the <0001> crystallographic axis parallel to the <0001> axis of the sapphire substrate, and the hexagonal basal in-planes of AlBN and β-Nb_2N are aligned with each other, and both at a 30° rotational offset with that of Al_2O_3.

2.2. Effect of MBE Growth Parameters on B Incorporation in AlBN

The effect of growth parameters on niobium nitride films has been explored before.[33] Keeping the same growth conditions for the β-Nb_2N, we vary the conditions for B incorporation in the AlBN/β-Nb_2N/Al_2O_3 heterostructures. We vary the substrate temperature and B flux via the B cell temperature. **Figure 2**a shows that the B flux from the effusion cell follows Arrhenius behavior with an activation energy of ≈5.17 eV, comparable to reports of ≈5.5 to 5.9 eV,[44–46] to be contrasted with ≈3.28 eV from the Al effusion cell, which is close to other reports of ≈3.16 eV/atom.[44]

We used XPS to obtain the composition of the AlBN films. Keeping the B cell temperature at 1850 °C, we used substrate growth temperatures of 600, 750, and 900 °C. Figure 2b shows the B composition in the AlBN layer with varying substrate temperature. With the AlBN growth temperature increase from 600 °C to 750 to 900 °C, the B content in the AlBN films decreases from 14.7% to 8% to 3.5%, as shown in Figure 2b. Then, keeping the substrate temperature at 750 °C we grew a series of samples

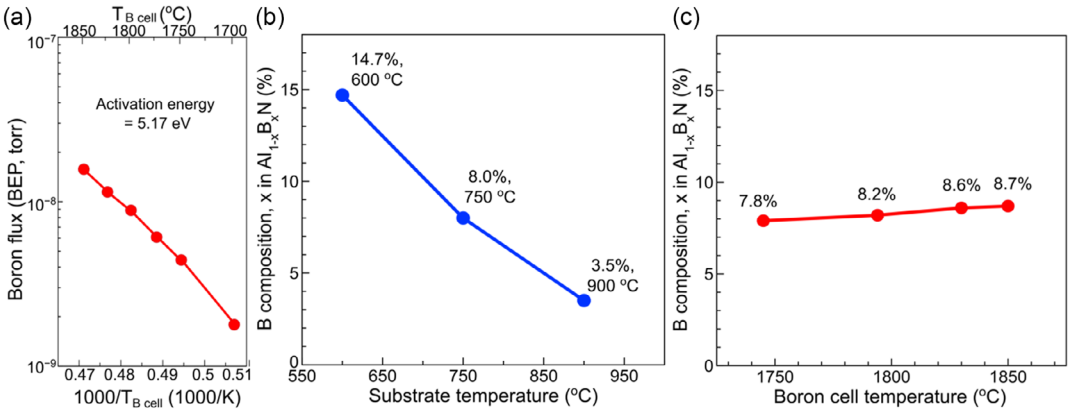

Figure 2. Effect of MBE growth parameters (Substrate, B cell temperature) on the composition of AlBN films grown on β-Nb_2N on sapphire. a) Arrhenius behavior of B cell temperature on B flux indicating that the B flux can be well controlled by B cell temperature b) B composition, *x*% of $Al_{1-x}B_xN$ films as a function of substrate thermocouple temperature, c) B composition, *x*% of $Al_{1-x}B_xN$ films as a function of boron Knudsen cell thermocouple temperature.

at different B fluxes. Figure 2c shows that the B content in the AlBN films increases only slightly from 7.8% to 8.7% for B cell temperature varying from 1742 to 1850 °C, causing the B flux to increase from $\approx 5 \times 10^{-9}$ to 1.5×10^{-8} torr. Thus, the B incorporation in the AlBN films is largely controlled by the substrate growth temperature, rather than by the supplied B flux species. The AlBN films grow in a reaction rate-controlled regime rather than a mass transport-controlled regime.

The wurtzite phase of $Al_{1-x}B_xN$ is predicted to be stable up to $x = 26\%$–28% B composition.[47] We only observed the wurtzite phase of AlBN by RHEED or XRD-RSM diffraction patterns for all films grown in this study, and no signature of layered hexagonal or cubic phases of AlBN. Photoelectron peaks corresponding to the sp^2-bonded layered hexagonal phase were not observed in the XPS spectra of AlBN films, which only showed B1*s*, N1*s*, and Al2*p* peaks without π plasmon loss peaks, a common feature observed in layered hexagonal BN.[48] The wurtzite phase of binary BN is expected to be stable at temperatures below ≈1000 to 1500 K (i.e., below ≈730 to 1230 °C), and the layered hexagonal (or cubic) phases are more stable at higher temperatures.[16,49,50] Thus, low growth temperatures favor B incorporation in the wurtzite form in the AlBN films and possibly suppress the conversion from wurtzite BN to hexagonal (or cubic) BN[49] as the B % is increased in the crystalline wurtzite films.

2.3. Structural Properties of AlBN

The ball and stick crystal structure model of a wurtzite AlBN cell in **Figure 3**a illustrates the c and a lattice parameters. We measured the lattice parameters of the β-Nb_2N and AlBN layers from XRD-RSM β-Nb_2N 103 and AlBN 103 Bragg reflections. The β-Nb_2N films showed out-of-plane c-lattice parameter of 4.96 Å and in-plane a-lattice parameter of 3.054 Å. Figure 3b shows the measured c-axis and a-axis lattice parameters of wurtzite $Al_{1-x}B_xN$ films as a function of the B compositions. With increasing B content, the out-of-plane c-lattice parameter decreases monotonically from the $c_{AlN} = 5.004$ Å to $c_{AlBN} = 4.967$ Å for 14.7% B. The in-plane a-parameter changes nonmonotonically with increasing B content, initially increasing from $a_{AlN} = 3.106$ Å to $a_{AlBN} = 3.145$ Å for $x = 3.5\%$ and decreasing to $a_{AlBN} = 3.099$ Å for 14.7% B. The wurtzite AlBN films with 0 to 14.7% B content have ≈1.1% to ≈2.8% in-plane lattice mismatch with the underlying β-Nb_2N layer.

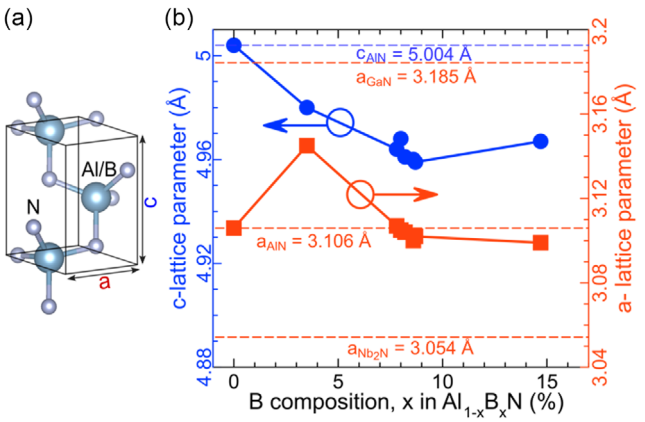

Figure 3. Structural c-, a-lattice parameters of AlBN films grown on β-Nb_2N/sapphire. a) Ball and stick crystal structure model of wurtzite AlBN showing c and a axis, orientations, lattice parameters, b) c-axis and a-axis lattice parameters of wurtzite AlBN films grown on nitrided sapphire as a function of B composition.

The c-parameter of AlBN films decreases with B incorporation. This is because of the small size of B compared to Al, and the expected c-parameter of 4.20 Å for wurtzite BN[16] is smaller than 5.004 Å of AlN. Substitution of B in the wurtzite AlN lattice is reported to locally distort the AlN_4 tetrahedra, leading to deviations in tetrahedral bond angles from the ideal 109.4°.[18,19] The vertical bonds in the ideal tetrahedra are reported to deflect away from the c-axis by as much as 13° for ≈22% B.[18,19] Such distortion of tetrahedral geometry towards trigonal planar or hexagonal structure should increase the in-plane a-parameter of AlN with up to ≈3% B incorporation.[18,19] The expected a-parameter 2.54 Å for the wurtzite BN[16] is smaller than 3.106 Å of AlN. Thus, the a-parameter decreases with increasing B content of the AlBN films from ≈3% to ≈14.7%.

Figure 4a shows a cross-section TEM image of the AlBN/β-Nb_2N/Al_2O_3 heterostructure sample with 14.7% B content. Sharp, abrupt interfaces are visible at the AlBN/β-Nb_2N and β-Nb_2N/Al_2O_3 heterojunctions. The AlBN film exhibits columnar crystal morphology, possibly arising from a three-dimensional growth mode common in N-rich growth conditions.[42] Figure 4b shows a HRTEM micrograph of the AlBN/β-Nb_2N heterojunction. The Fast Fourier transforms (FFT) of regions: i and ii) enclosing the heterostructure as marked by square red and blue boxes in the AlBN and β-Nb_2N films respectively in Figure 4c and d, respectively, show <0002> spots in the $[1\bar{1}00]$ projection as confirmed by the simulated diffraction patterns for wurtzite AlBN and hexagonal β-Nb_2N along $[1\bar{1}00]$ zone axis. They confirm the wurtzite phase of AlBN and the hexagonal phase of β-Nb_2N. Similar $[1\bar{1}00]$ projection axes of AlBN film and β-Nb_2N films suggest an epitaxial relationship between the layers. Figure 4e shows a higher magnification image of bulk AlBN, where no signs of a secondary phase were observed.

2.4. Ferroelectric AlBN/Superconducting Nb_2N Heterostructure

Piezo-response force microscopy (PFM) at 300 kHz frequency was performed at room temperature on the AlBN/β-Nb_2N/Al_2O_3 heterostructure sample containing ≈4% B using the bottom metallic β-Nb_2N electrode contacted with Ag paste, and the PFM conductive tip as the top electrode. **Figure 5**a shows the butterfly-shaped amplitude curves and Figure 5b shows the box-shaped hysteretic phase loops indicating ferroelectricity of the AlBN film. These loops showing ≈180° phase difference at zero voltage were repeatable over several measurements, indicating the external electric field reversibly and repeatedly switches the AlBN film between states of opposite polarity. The PFM phase hysteresis measurements indicate a coercive field E_C ≈ 0.72 MV cm^{-1} for the MBE-grown AlBN films, smaller than reported in sputtered AlBN layers. While the polarization switching in the MBE-grown AlBN films is unmistakable, the leakage currents and incomplete wake-up currently limit the maximum electric fields that can be applied for switching to a smaller coercive field than the sputtered layers.[9,51,52] Wet KOH etching of

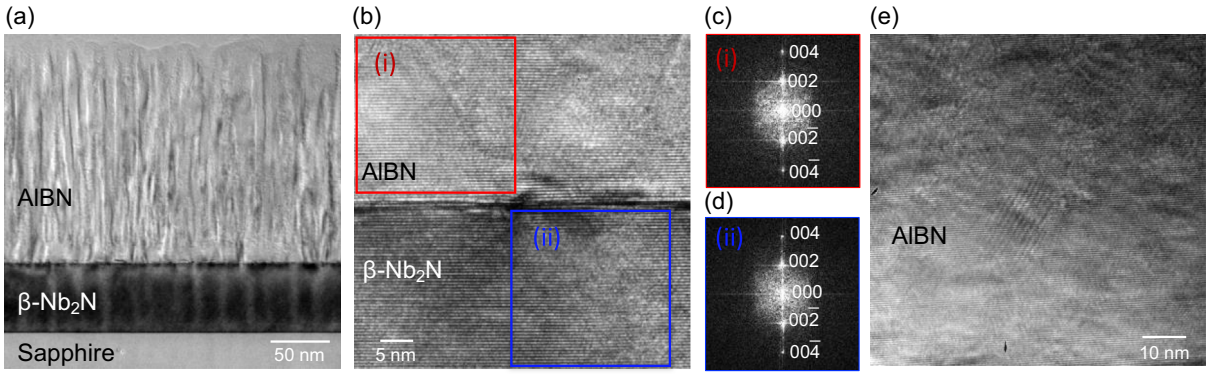

Figure 4. TEM micrographs and FFTs of 14.7% B containing AlBN/ β-Nb_2N/ Al_2O_3 heterostructure. a,b) TEM micrographs at a higher magnification with marked regions i), ii) used for FFT analysis c,d) FFT of red and blue marked regions-1, 2 indicating wurtzite phase of AlBN and hexagonal phase of β-Nb_2N and e) A HRTEM image of bulk AlBN film.

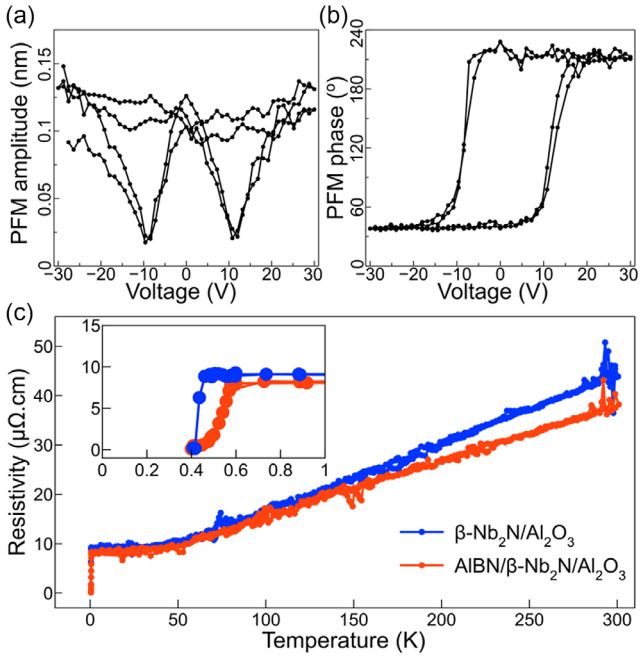

Figure 5. Ferroelectric AlBN/superconducting β-Nb_2N heterostructure. a) Butterfly PFM Amplitude and b) hysteretic PFM Phase loops in MBE AlBN/Nb_2N heterostructure indicating ferroelectric nature of AlBN films, and c) Metallic, and superconducting nature of β-Nb_2N films with $\rho_{298K} = 37–45\ \mu\Omega\,cm^{-1}$ and T_C of ≈0.4–0.6 K. A reference β-Nb_2N film grown on Al_2O_3 as well as a the β-Nb_2N film in the AlBN/β-Nb_2N/ Al_2O_3 heterostructure show superconducting nature of β-Nb_2N films. The superconductivity of β-Nb_2N is preserved after the subsequent AlBN film growth.

the PFM-poled AlBN/Nb_2N film sample shows different etching rates at oppositely poled regions, i.e., the nitrogen polar regions etched at a higher rate than metal polar regions[12,53–55] (see Supporting Information). This further demonstrates that the polarization of the AlBN films can be switched between the states of opposite polarities by an external field, and the AlBN films are indeed ferroelectric.

Temperature-dependent electronic resistivity data of reference β-Nb_2N film grown on Al_2O_3 without the top AlBN film and the AlBN/β-Nb_2N/Al_2O_3 heterostructure are shown in Figure 5c and its inset. The reference β-Nb_2N/Al_2O_3 film showed a room temperature resistivity $\rho = 42–49\ \mu\Omega\,cm$ and a superconducting transition temperature $T_C = 0.41$ K. The β-Nb_2N film in the AlBN/β-Nb_2N/Al_2O_3 heterostructure showed a room temperature resistivity $\rho = 37–46\ \mu\Omega\,cm$ and a superconducting critical transition temperature T_C ≈0.4–0.6 K, indicating that the β-Nb_2N phase and superconducting properties are preserved in the heterostructure after the AlBN growth. This is feasible because β-Nb_2N is thermodynamically stable below the MBE growth temperatures of AlN/AlBN (≈900 °C).[33-36] The superconductivity of β-Nb_2N is preserved even after the subsequent AlBN film growth. The realization of all epitaxial AlBN/β-Nb_2N nitride heterostructures with ferroelectricity and superconductivity opens the possibility for novel devices.

3. Summary

Epitaxial growth of AlBN/β-Nb_2N heterostructures with B compositions from 0 to ≈15% was demonstrated by nitrogen PAMBE on c-plane sapphire substrates. The AlBN films show a single wurtzite phase crystal structure with at least up to ≈15% B content. Wurtzite AlBN and hexagonal β-Nb_2N films grow epitaxially along the <0001> crystallographic directions on the c-plane sapphire substrate. The hexagonal basal in-planes of AlBN and β-Nb_2N have a zero-degree rotational mismatch; they are at 30° alignment to the hexagonal basal plane of Al_2O_3 substrate. The AlBN film grows in a reaction rate-controlled regime, with the B content in the AlBN films increasing from 3.5% to 14.7% with a decrease in the growth temperature; B flux had a weak effect on the B content in the AlBN films. With increasing B content in the AlBN films, the c parameter decreases monotonically while a nonmonotonic trend is observed in the in-plane a parameter. The AlBN films with 0%–15% B show an in-plane lattice mismatch of ≈1.1% to 2.8% with the underlying β-Nb_2N layers. HRTEM reveals sharp, abrupt interfaces at AlBN/β-Nb_2N and β-Nb_2N/Al_2O_3 heterojunctions. MBE-grown AlBN films exhibit ferroelectricity, and the β-Nb_2N shows a room temperature

resistivity $\rho = 37–45\ \mu\Omega\,\text{cm}$ and a superconducting critical transition temperature $T_C = \approx 0.4–0.6\ \text{K}$. To the best of our knowledge, this is the first realization of an all epitaxial ferroelectric-superconductor nitride heterostructure. Such heterojunctions could be useful for Josephson junctions of use for classical and quantum computing devices, adding to existing polar AlN, and metallic, superconducting hexagonal β-Nb_2N heterostructures.[34,35] Adding ferroelectric layers can enable nonvolatile, programmable superconducting electronic devices and the ferroelectric polarization control of superconductivity.[28-32] AlBN/β-Nb_2N nitride heterostructures can be used in classical and quantum acoustodynamic electronics based on nitride materials.

4. Experimental Section

A Veeco GenXplor nitrogen plasma-assisted molecular beam epitaxy (PAMBE) system with an idle base pressure of 10^{-9} torr was used to perform all the growths for this study. A niobium source of 99.9999% purity was loaded in a tungsten crucible and evaporated from a Telemark electron beam evaporation system. An aluminum source of 99.9999% purity from United Mineral & Chemical Corp (UMC) was loaded in a PBN crucible and evaporated using Knudsen effusion cells. A boron source of 99.9999% purity from UMC was loaded in a pyrolytic graphite liner inside a tungsten crucible and evaporated using a high-temperature Knudsen effusion cell. Active nitrogen species were supplied using a Veeco RF UNI-Bulb plasma source with 99.99995% purity nitrogen gas at a 1.95 sccm flow rate and with an RF plasma operating at 200 W RF power and the chamber pressure was $\approx 2 \times 10^{-5}$ torr during growth. The average growth rates for the β-Nb_2N films and AlBN films were ≈ 2.4 and $\approx 3.1\ \text{nm min}^{-1}$, respectively. The substrate thermocouple temperature was calibrated using a gallium droplet desorption test, where Ga flux was supplied from the Knudsen effusion cell. Heying et al. have reported that Ga desorption from a GaN surface follows an Arrhenius behavior, as indicated by equation (1) where k_B is the Boltzmann constant in eV, and T is the substrate temperature in Kelvin.[56] The measured Ga desorption flux from a GaN surface as a function of substrate thermocouple temperature was fitted to Arrhenius equation (2) where ΔT is determined to be ≈49.5 °C. Thus, the actual surface temperature[56] is ≈50 °C higher than the measured substrate thermocouple temperature. In situ monitoring of the growth surface was performed using a KSA Instruments reflection high-energy electron diffraction (RHEED) apparatus with a Staib electron gun operating at 14.5 kV and 1.45 A

$$\text{Ga flux}\,(\text{nm min}^{-1}) = (2.2 \times 10^{15}\ \text{nm min}^{-1}) \times \exp\left(\frac{-2.832\ \text{eV}}{k_B \times (T)}\right) \quad (1)$$

$$\text{Ga flux}\,(\text{nm min}^{-1}) = (2.2 \times 10^{15}\ \text{nm min}^{-1}) * \exp\left(\frac{-2.832\ \text{eV}}{k_B \times (T + \Delta T)}\right) \quad (2)$$

Asylum Research Cypher ES system was used to perform atomic force microscopy (AFM) imaging in a tapping mode. Film crystal structure, phase, and orientation were characterized using a PANalytical Empyrean diffractometer at 45 kV, 40 mA with Cu Kα, 1.5406 Å radiation. X-Ray diffraction (XRD) reciprocal space map (RSM) and symmetric phi scans of asymmetric Bragg reflections were measured. Compositions of the AlBN films were analyzed with a Scienta-Omicron ESCA-2SR X-Ray photoelectron spectroscopy (XPS) instrument equipped with an Al Kα (1486.6 eV) source. Adventitious carbon and native oxide were removed from the sample surface using an Ar^+ ion beam. A hemispherical analyzer collected the photoelectrons with a pass energy of 58.7 eV. Prolonged high-resolution C1s, B1s, Al2*p*, and N1s core-level X-Ray photoelectron spectra were collected to obtain a high signal-to-noise ratio.

Cross-sectional samples for transmission electron microscopy (TEM) were prepared by focused ion beam milling using a Thermo Fisher Helios 5UX dual-beam instrument with initial thinning done at 30 keV and further thinning at 5 and 2 keV. An image-corrected FEI Titan 80–300 operated at 300 kV was used to record the high-resolution TEM images. The piezo force microscopy (PFM) measurements were performed at an AC voltage of 2 V and at a 300 kHz measurement frequency using the Asylum Research Cypher ES system. A triangular-square waveform pulse with 0.1 Hz was used to perform PFM measurements with a 25 ms bias-on state for writing and a 25 ms bias-off state for reading. The PFM phase and amplitude and phase loops were acquired in the bias-off read state. The superconducting transition temperatures of β-Nb_2N films were measured by performing temperature-dependent resistance measurements in a Quantum Design Physical Property Measurement System (PPMS) with the Helium-3 refrigerator.

Supporting Information

Supporting Information is available from the Wiley Online Library or from the author.

Acknowledgements

This work was partly supported by SUPREME, one of seven centers in JUMP 2.0, a Semiconductor Research Corporation (SRC) program sponsored by DARPA (epitaxy); the Ultra Materials for a Resilient Energy Grid (ULTRA), an Energy Frontier Research Center (EFRC) funded by the U.S. Department of Energy, Office of Science, Basic Energy Sciences under award no. DE-SC0021230 (structural characterization), and supported by the Army Research Office (ARO) grant no. W911NF2220177 (other characterizations). This work made use of the Cornell Center for Materials Research (CCMR) Shared Facilities, which are supported through the NSF MRSEC Program under grant no. DMR-1719875 ; the Cornell NanoScale Facility, a member of the National Nanotechnology Coordinated Infrastructure (NNCI), supported by the National Science Foundation (grant no. NNCI-2025233); the John M. Cowley Center for High-Resolution Electron Microscopy at Arizona State University; and the Platform of Accelerated Realization, Analysis, and Discovery of Interface Materials (PARADIM), which is supported by the National Science Foundation under cooperative agreement no. DMR-2039380.

Conflict of Interest

The authors declare no conflict of interest.

Data Availability Statement

The data that support the findings of this study are available from the corresponding author upon reasonable request.

Keywords

AlBN, aluminum boron nitride, epitaxial growth, ferroelectric, group-III nitrides, molecular beam epitaxy, Nb_2N, niobium nitride, semiconductors, superconductor, transition metal nitride, ultrawide bandgap

Received: May 1, 2024
Revised: July 5, 2024
Published online:

[1] D. Jena, R. Page, J. Casamento, P. Dang, J. Singhal, Z. Zhang, J. Wright, G. Khalsa, Y. Cho, H. G. Xing, *Jpn. J. Appl. Phys.* **2019**, *58*, SC0801.
[2] I. Akasaki, *Rev. Mod. Phys.* **2015**, *87*, 1119.
[3] H. Amano, *Rev. Mod. Phys.* **2015**, *87*, 1133.
[4] S. Nakamura, *Rev. Mod. Phys.* **2015**, *87*, 1139.
[5] S. T. Haider, M. A. Shah, D.-G. Lee, S. Hur, *IEEE Access* **2023**, *11*, 58779.
[6] M. Kneissl, J. Rass, in *III-Nitride Ultraviolet Emitters: Technology and Applications*, Springer International Publishing, Cham **2016**.
[7] H. Amano, R. Collazo, C. D. Santi, S. Einfeldt, M. Funato, J. Glaab, S. Hagedorn, A. Hirano, H. Hirayama, R. Ishii, Y. Kashima, Y. Kawakami, R. Kirste, M. Kneissl, R. Martin, F. Mehnke, M. Meneghini, A. Ougazzaden, P. J. Parbrook, S. Rajan, P. Reddy, F. Römer, J. Ruschel, B. Sarkar, F. Scholz, L. J. Schowalter, P. Shields, Z. Sitar, L. Sulmoni, T. Wang, et al., *J. Phys. D: Appl. Phys.* **2020**, *53*, 503001.
[8] K. H. Ye, G. Han, I. W. Yeu, C. S. Hwang, J.-H. Choi, *Phys. Status Solidi RRL* **2021**, *15*, 2100009.
[9] J. Hayden, M. D. Hossain, Y. Xiong, K. Ferri, W. Zhu, M. V. Imperatore, N. Giebink, S. Trolier-McKinstry, I. Dabo, J.-P. Maria, *Phys. Rev. Mater.* **2021**, *5*, 044412.
[10] J. Casamento, K. Nomoto, T.-S. Nguyen, H. Lee, C. Savant, L. Li, A. Hickman, T. Maeda, Y.-T. Shao, J. Encomendero, V. Gund, T. Vasen, S. Afroz, D. Hannan, D. A. Muller, H. G. Xing, D. Jena, in *2023 IEEE BiCMOS and Compound Semiconductor Integrated Circuits and Technology Symp. (BCICTS)*, IEEE, Monterey, CA, USA **2023**, pp. 132–136.
[11] P. Wang, D. Wang, S. Mondal, M. Hu, J. Liu, Z. Mi, *Semicond. Sci. Technol.* **2023**, *38*, 043002.
[12] S. Fichtner, N. Wolff, F. Lofink, L. Kienle, B. Wagner, *J. Appl. Phys.* **2019**, *125*, 114103.
[13] D. Wang, S. Mondal, J. Liu, M. Hu, P. Wang, S. Yang, D. Wang, Y. Xiao, Y. Wu, T. Ma, Z. Mi, *Appl. Phys. Lett.* **2023**, *123*, 033504.
[14] J. Casamento, K. Nomoto, T. S. Nguyen, H. Lee, C. Savant, L. Li, A. Hickman, T. Maeda, J. Encomendero, V. Gund, A. Lal, J. C. M. Hwang, H. G. Xing, D. Jena, in *2022 Int. Electron Devices Meeting (IEDM)*, IEEE, San Fransisco, **2022**, pp. 11.1.1–11.1.4.
[15] J. Casamento, T.-S. Nguyen, Y. Cho, C. Savant, T. Vasen, S. Afroz, D. Hannan, H. G. Xing, D. Jena, *Appl. Phys. Lett.* **2022**, *121*, 192101.
[16] R. Kudrawiec, D. Hommel, *Appl. Phys. Rev.* **2020**, *7*, 041314.
[17] J.-X. Shen, D. Wickramaratne, C. G. Van De Walle, *Phys. Rev. Mater.* **2017**, *1*, 065001.
[18] C. Milne, T. Biswas, A. K. Singh, *Adv. Electron. Mater.* **2023**, *9*, 2201197.
[19] A. Suceava, J. Hayden, K. P. Kelley, Y. Xiong, B. Fazlioglu-Yalcin, I. Dabo, S. Trolier-McKinstry, J.-P. Maria, V. Gopalan, *Opt. Mater. Express* **2023**, *13*, 1522.
[20] C. Savant, K. Nomoto, T.-S. Nguyen, Y.-H. Chen, R. Page, H. G. Xing, D. Jena, in *Electronic Materials Conf. 65 (EMC)*, Underline Science Inc., Santa Barbara, CA, USA **2023**.
[21] G. A. Alvarez, J. Casamento, L. Van Deurzen, M. I. Khan, K. Khan, E. Jeong, E. Ahmadi, H. G. Xing, D. Jena, Z. Tian, *Mater. Res. Lett.* **2023**, *11*, 1048.
[22] Y. Utsumi, T. Imai, N. Fujimori, US Patent 5,766,783, **1998**.
[23] N. N. Greenwood, A. Earnshaw, in *Chemistry of the Elements*, Butterworth-Heinemann, Oxford **1997**, pp. 944–953.
[24] J. Casamento, H. G. Xing, D. Jena, *Phys. Status Solidi B* **2020**, *257*, 1900612.
[25] A. H. El-ladan, S. Subramani, *Appl. Phys. A* **2021**, *127*, 540.
[26] A. N. Caruso, *J. Phys.: Condens. Matter* **2010**, *22*, 443201.
[27] M. Schieber, E. Mojaev, M. Roth, A. Zuck, O. Khakhan, A. Fleider, *Nucl. Instrum. Methods Phys. Res., Sect. A* **2009**, *607*, 634.
[28] M. Suleiman, M. F. Sarott, M. Trassin, M. Badarne, Y. Ivry, *Appl. Phys. Lett.* **2021**, *119*, 112601.
[29] A. Crassous, R. Bernard, S. Fusil, K. Bouzehouane, J. Briatico, M. Bibes, A. Barthélémy, J. E. Villegas, *J. Appl. Phys.* **2013**, *113*, 024910.
[30] A. Crassous, R. Bernard, S. Fusil, K. Bouzehouane, D. Le Bourdais, S. Enouz-Vedrenne, J. Briatico, M. Bibes, A. Barthélémy, J. E. Villegas, *Phys. Rev. Lett.* **2011**, *107*, 247002.
[31] C. H. Ahn, S. Gariglio, P. Paruch, T. Tybell, L. Antognazza, J.-M. Triscone, *Science* **1999**, *284*, 1152.
[32] K. S. Takahashi, M. Gabay, D. Jaccard, K. Shibuya, T. Ohnishi, M. Lippmaa, J. M. Triscone, *Nature* **2006**, *441*, 195.
[33] J. G. Wright, H. G. Xing, D. Jena, *Phys. Rev. Mater.* **2023**, *7*, 074803.
[34] N. Nepal, D. S. Katzer, D. J. Meyer, B. P. Downey, V. D. Wheeler, D. F. Storm, M. T. Hardy, *Appl. Phys. Express* **2016**, *9*, 021003.
[35] A. Kobayashi, S. Kihira, T. Takeda, M. Kobayashi, T. Harada, K. Ueno, H. Fujioka, *Adv. Mater. Int.* **2022**, *9*, 2201244.
[36] W. Lengauer, M. Bohn, B. Wollein, K. Lisak, *Acta Mater.* **2000**, *48*, 2633.
[37] V. K. Gupta, C. C. Wamsley, M. W. Koch, G. W. Wicks, *J. Vac. Sci. Technol., B: Microelectron. Nanometer Struct. Process., Meas., Phenom.* **1999**, *17*, 1246.
[38] R. Cramer, Ph.D. Thesis, University of California, Santa Barbara **2019**.
[39] T. L. Williamson, N. R. Weisse-Bernstein, M. A. Hoffbauer, *Phys. Status Solidi C* **2014**, *11*, 462.
[40] W. E. Hoke, A. Torabi, J. J. Mosca, T. D. Kennedy, *J. Vac. Sci. Technol., B: Microelectron. Nanometer Struct.* **2007**, *25*, 978.
[41] J. G. Wright, C. S. Chang, D. A. Muller, H. G. Xing, D. Jena, *APL Mater.* **2022**, *10*, 051103.
[42] M. Henini, in *Molecular Beam Epitaxy: From Research to Mass Production*, Newnes, Elsevier **2012** ISBN: 9780123878397.
[43] J. Casamento, V. Gund, H. Lee, K. Nomoto, T. Maeda, B. Davaji, M. J. Asadi, J. Wright, Y.-T. Shao, D. A. Muller, A. Lal, D. Jena, arXiv preprint arXiv:2105.10114 **2021**.
[44] R. E. Honig, *RCA Rev.* **1957**, *28*, 195.
[45] A. W. Searcy, C. E. Myers, *J. Phys. Chem.* **1957**, *61*, 957.
[46] G. Verhaegen, J. Drowart, *J. Chem. Phys.* **1962**, *37*, 1367.
[47] Y. Hasegawa, T. Akiyama, A.-M. Pradipto, K. Nakamura, T. Ito, *Jpn. J. Appl. Phys.* **2019**, *58*, SCCB21.
[48] R. Page, J. Casamento, Y. Cho, S. Rouvimov, H. G. Xing, D. Jena, *Phys. Rev. Mater.* **2019**, *3*, 064001.
[49] F. R. Corrigan, F. P. Bundy, *J. Chem. Phys.* **1975**, *63*, 3812.
[50] L. Vel, G. Demazeau, J. Etourneau, *Mater. Sci. Eng., B* **1991**, *10*, 149.
[51] W. Zhu, F. He, J. Hayden, Z. Fan, J. I. Yang, J. Maria, S. Trolier-McKinstry, *Adv. Electron. Mater.* **2022**, *8*, 2100931.
[52] C. Savant, V. Gund, K. Nomoto, T. Maeda, S.Jadhav, J. Lee, M. Ramesh, E. Kim, T.S. Nguyen, Y.H. Chen, J. Casamento, F. Rana, A. Lal, H.G. Xing, and D. Jena, *Appl. Phys. Lett.* **2024**, https://doi.org/10.1063/5.0181217.
[53] A. N. Mariano, R. E. Hanneman, *J. Appl. Phys.* **1963**, *34*, 384.
[54] D. Zhuang, J. H. Edgar, *Mater. Sci. Eng., R* **2005**, *48*, pp. 1–46.
[55] M. Bickermann, S. Schmidt, B. M. Epelbaum, P. Heimann, S. Nagata, A. Winnacker, *J. Cryst. Growth* **2007**, *300*, 299.
[56] B. Heying, R. Averbeck, L. F. Chen, E. Haus, H. Riechert, J. S. Speck, *J. Appl. Phys.* **2000**, *88*, 1855.